CCS Chemistry

RESEARCH ARTICLE

Received: Nov. 8, 2020 | Accepted: Dec. 16, 2020

CrN-Encapsulated Hollow Cr-N-C Capsules Boosting Oxygen Reduction Catalysis in PEMFC

Hui Yang[1], Xu Wang[2], Tao Zheng[3], Nelly Cantillo Cuello[4], Gabriel Goenaga[4], Thomas A. Zawodzinski[4], He Tian[2]*, Joshua T. Wright[5], Robert W. Meulenberg[6], Xiangke Wang[1]*, Zhenhai Xia[3] & Shengqian Ma[7]*

[1]*College of Environmental Science and Engineering, North China Electric Power University, Beijing 102206,* [2]*State Key Laboratory of Silicon Materials, Center of Electron Microscopy, School of Materials Science and Engineering, Zhejiang University, Hangzhou 310027,* [3]*Department of Materials Science and Engineering, University of North Texas, Denton, TX 76203,* [4]*Chemical and Biomolecular Engineering Department, University of Tennessee, Knoxville, TN 37996,* [5]*Department of Physics, Illinois Institute of Technology, Chicago, IL 60616,* [6]*Department of Physics and Astronomy, Frontier Institute for Research in Sensor Technologies, University of Maine, Orono, ME 04469,* [7]*Department of Chemistry, University of North Texas, Denton, TX 76201*

**Corresponding authors: Shengqian.Ma@unt.edu; xkwang@ncepu.edu.cn; hetian@zju.edu.cn*

Cite this: *CCS Chem.* **2021**, *3*, 208–218

Understanding the origin of the catalytic activity for the development of efficient catalysts is critical yet challenging. Herein, we report a simple strategy for the synthesis of chromium nitride nanoparticles (CrNNPs) encapsulated into hollow chromium–nitrogen–carbon capsules (CrN@H-Cr-N_x-C). The CrN@H-Cr-N_x-C demonstrated excellent electrocatalytic activity for the oxygen reduction reaction (ORR) in acidic solutions. When applied as a cathode material in a proton-exchange membrane fuel cell (PEMFC), the CrN@H-Cr-N_x-C achieved outstanding initial performance, which is better than that of the PEMFC with H-Cr-N_x-C cathode material. The CrN@H-Cr-N_x-C cathode also showed good stability over 110 h of operation. These results demonstrated that the coexistence of atomically dispersed CrN_x sites and sufficient CrNNPs is essential for excellent PEMFC performances. Density functional theory (DFT) studies further corroborated that CrNNPs can boost the ORR activity of H-Cr-N_x-C. This finding opens a new avenue for the fabrication of low-cost, highly active, and durable ORR catalysts for PEMFC and other applications.

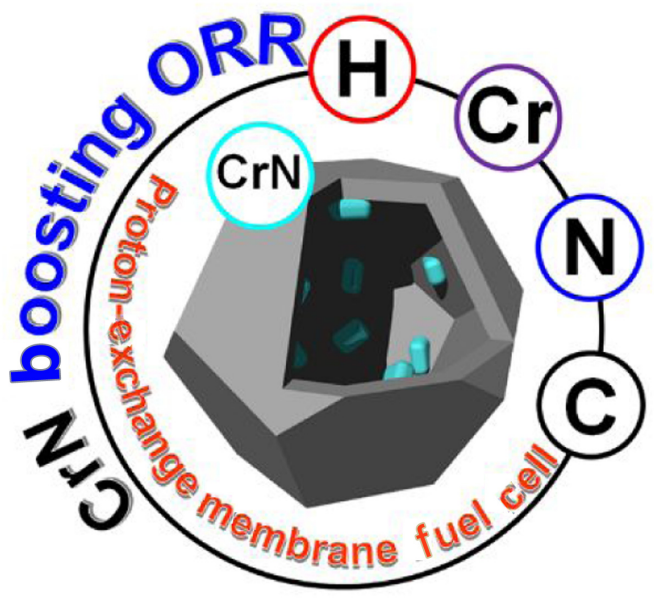

Keywords: chromium–nitrogen–carbon, fuel cell, chromium nitride, metal–organic framework, durability

DOI: 10.31635/ccschem.020.202000645
CCS Chem. **2021**, *3*, 208–218

Introduction

The emergence of the proton-exchange membrane fuel cell (PEMFC) has provided enormous opportunities to develop the next generation of power sources for electric vehicles due to advantages such as high energy conversion efficiency and environmental protection.[1,2] However, the widespread use of PEMFC is currently limited by the scarcity and high cost of platinum-group metal (PGM) electrocatalysts, particularly on the cathode.[3–7] Since the oxygen reduction reaction (ORR) plays a crucial role in the PEMFC, a significant amount of effort have been devoted to the search for a PGM-free ORR catalyst in acidic solutions, and great progress has been made.

To address the above issues, porous carbons decorated with atomically dispersed transition metal–nitrogen (M–N_x–C; M = Fe, Co, and Mn) moieties have emerged as high-performance ORR electrocatalytic catalysts for PEMFC in acidic solutions.[8–22] It is generally believed that the catalysis occurs on the exposed MN_x active sites of the M–N_x–C catalysts, and increasing the density of MN_x moieties while minimizing other metal-based phases is an effective strategy for improving the catalytic activity. Thus, many efforts have been paid to identifying more active MN_x coordination configurations.[23–33] However, the interactive catalytic contribution of the metal-based phases (nanoparticles and/or clusters) from aggregation has received less focus and needs further exploration.[34–41] Besides the activity, the performance of a PEMFC with M–N_x–C catalysts as cathode typically degrades rapidly (~40–80%) in the first 100 h of testing in PEMFC.[42–44] Among studied M–N_x–C catalysts, Fe–N_x–C has been the most widely studied because of their high activity for ORR in PEMFC. Nevertheless, the atomically dispersed FeN_x center suffers a serious stability issue from oxidative corrosion via Fenton reaction.[42,43,45–48] In these cases, the design and preparation of highly active, durable, PGM-free catalysts, as well as understanding their origin of catalytic activity, are still one of the long-standing challenges in PEMFC engineering.

In this work, we report that the chromium nitride nanoparticles (CrNNPs) encapsulated into hollow chromium–nitrogen–carbon capsules (denoted as CrN@H–Cr–N_x–C) were successfully prepared by pyrolysis of a ZIF-8@chromium–tannic acid (ZIF-8@Cr–TA) core–shell nanocrystals. On account of the enriched CrN_x sites, sparse CrNNPs, and abundant micro/mesopores, CrN@H–Cr–N_x–C exhibited outstanding electrocatalytic activity for ORR in an acidic solution. Subsequently, the CrN@H–Cr–N_x–C demonstrated an excellent open-circuit voltage (OCV) and high current and power densities when used as a cathode catalyst in PEMFC. Durability tests indicated that the CrN@H–Cr–N_x–C catalyst has very promising stability over 110 h of operation. The H–Cr–N_x–C showed lower activities compared with the CrN@H–Cr–N_x–C counterpart. The benefits of encapsulated CrNNPs to boost ORR performance of CrN@H–Cr–N_x–C were confirmed by density functional theory (DFT) calculations. Our work opens a new avenue for the rational development of more economical catalysts for PEMFC.

Experimental Methods

General procedure for preparation of ZIF-8@K–TA composite

ZIF-8@K–TA was synthesized by following our reported procedure.[24] Typically, 200 mg of ZIF-8 nanocrystals was dispersed in 10 mL of deionized water. Separately, 3 mL of TA aqueous solution (24 mM, pH 8 adjusted by 6 M KOH) was added to the above ZIF-8 suspension. The mixture was then stirred for 5 min. The precipitates were centrifuged, washed with methanol three times, and dried in an oven at 40 °C.

Preparation of ZIF-8@Cr–TA composite

In a typical procedure, 30 mL of a methanolic solution containing obtained ZIF-8@K–TA and 200 mg of $Cr(NO_3)_3{\cdot}9H_2O$ was stirred for 3 h. The solid product was centrifuged, washed with methanol three times, and dried in an oven at 40 °C. ZIF-8@Cr–TA(100) composite was synthesized via a similar synthetic procedure, only reducing the amount of $Cr(NO_3)_3{\cdot}9H_2O$ to 100 mg.

Preparation of CrN@H–Cr–N_x–C and H–Cr–N_x–C catalysts

In a typical procedure, the ZIF-8@Cr–TA(200) core–shell nanoparticles were heated to 900 °C with a ramp rate of 2 °C·min^{-1} under a nitrogen flow. Atter continuing pyrolyzed at 900 °C for 3 h, the black powder was obtained. Subsequently, the product was then immersed in 3 M H_2SO_4 at 90 °C for 12 h, then separated by filtration and washed thoroughly until the filtrate became neutral, and dried in an oven at 40 °C. The black powder was pyrolyzed at 900 °C for 3 h under a nitrogen flow. Waiting for the furnace cooling to room temperature, the final product (CrN@H–Cr–N_x–C) was obtained. H–Cr–N_x–C was prepared from the ZIF-8@Cr–TA(100) using the same protocol.

Other instrumentation, characterization methods, and experimental details, including material synthesis, rotating ring-disk electrode (RRDE) tests, membrane electrode assembly (MEA) preparation and single fuel cell tests, X-ray absorption fine structure (XAFS) measurements, and DFT calculations, are available in the Supporting Information.

DOI: 10.31635/ccschem.020.202000645
CCS Chem. **2021**, *3*, 208–218

Results and Discussion

The preparation of CrN@H-Cr-N_x-C essentially involves a three-step process (Scheme 1): (step I) uniform coating of the ZIF-8 template with K-TA polymer yield ZIF-8@K-TA core-shell structure[49]; (step II) replacement of the potassium cations in the K-TA shell by Cr(III) resulted in ZIF-8@Cr-TA; powder X-ray diffraction (PXRD) patterns, scanning electron microscopy (SEM) images, and energy-dispersive X-ray spectroscopy (EDXS) spectra showed the crystallinity of the ZIF-8 core, and dodecahedral morphology was retained, as expected (Supporting Information Figures S1–S4). The amorphous Cr-TA shell layer with ~10 nm thickness remained with the ZIF-8 core as confirmed by transmission electron microscopy (TEM; Supporting Information Figure S4b). (step III) Upon pyrolysis and acid etching, the ZIF-8@Cr-TA carbonized into hollow N-doped carbon capsules, and the coordinated Cr^{3+} ions were transformed into atomically dispersed $CrN(C)_x$ moieties anchored on carbon shell, as well as CrNNPs support on the internal surface simultaneously. The broad peak detected in the PXRD pattern of CrN@H-Cr-N_x-C at 24.7 can be attributed to the graphitic (002) reflection from the carbon (Figure 1a). The sharp diffraction peaks at 37.47, 43.54, 63.27, and 75.91 can be assigned to the (111), (200), (220), and (311) reflections for cubic CrN, suggesting that phase nitride was formed during pyrolysis. SEM and TEM images of CrN@H-Cr-N_x-C showed hollow capsule-like morphology with embedded large CrNNPs (Figures 1b and Supporting Information Figure S6). This suggested the chromium ions in the TA layer randomly aggregated into surface-supported nanoparticles in the capsule-forming step during heat treatment. Aberration-corrected high-angle annular dark-field scanning TEM (HAADF-STEM) was further used to investigate the chromium-containing hollow capsule. The fringes with a lattice spacing of 0.21 and 0.24 nm can be indexed to the (200) and (111) planes of cubic CrN, respectively (Figure 1c). Low magnification HAADF-STEM images and EDXS mappings of CrN@H-Cr-N_x-C illustrate the distribution of the C, N, and Cr species in both nanocrystals and hollow capsules (Figures 1d–1h). In addition to CrNNPs, a large number of prominent and isolated bright spots are evident against a dark background, suggesting the atomically dispersed chromium moieties anchor on the capsules (Figure 1g).

To further probe the atomically dispersed chromium moieties in CrN@H-Cr-N_x-C, we prepared the H-Cr-N_x-C under similar synthetic procedures, only reducing the Cr^{3+} content in ZIF-8@Cr-TA polymer (see the details in the Supporting Information). The CrN diffraction peaks disappeared in the PXRD pattern, indicated no crystalline CrN formed in H-Cr-N_x-C (Figure 1a). No obvious aggregation of chromium atoms could be found in the TEM image (Figure 2a). Aberration-corrected HAADF-STEM (Figures 2b–2d) and corresponding EDXS mapping images (Figures 2e–2i) further showed the high density of atomically dispersed (highlighted by red and yellow circles) chromium sites well anchored on the hollow N-doped carbon capsules. Taking into account these results together, we concluded that chromium ions tend to be more likely involved in the formation of atomically dispersed chromium sites anchored on hollow N-doped carbon capsules before they aggregated. However, if the chromium ions concentration is high enough, in addition to the formation of isolated $CrN(C)_x$ species, the rest aggregates to produce CrNNPs during pyrolysis.

The X-ray photoelectron spectroscopy (XPS) spectra of CrN@H-Cr-N_x-C are shown in Figures 3a and 3b and Supporting Information Figure S11. In the Cr 2p region, the XPS spectrum provides clear signals at 577.3 and 586.8 eV due to Cr $2p_{3/2}$ and Cr $2p_{1/2}$, attributed to chromium(III) (Figure 3a).[50,51] No metallic chromium was detected by XPS. The N 1s XPS spectrum can be deconvoluted into four components, pyridinic-N (398.5 eV), pyrrolic-N (399.2 eV), graphitic-N (400.9 eV), and quaternary-N (404.5 eV) (Figure 3b).[24] Pyridinic and pyrrolic nitrogen atoms doped into carbon shells can serve as the anchor points for trapping atomically dispersed chromium(III) ions via coordination bonds. These XPS results suggest that a portion of chromium(III) bonded with N-formed CrN nanoparticles. The rest of chromium(III) occupy sites in the N-doped carbon shell, similar to molecular species chromium porphyrins. The XPS spectra of H-Cr-N_x-C were very similar to those of CrN@H-Cr-N_x-C evaluated under the same test environments (Figures 3c and 3d and Supporting Information Figure S12).

X-ray absorption near-edge structure (XANES) and extended XAFS (EXAFS) measurements were further employed to probe the possible atomic structures of chromium sites in the catalysts. Cr foil, Cr_2O_3, and Cr_3C_2 were also analyzed as references. Normalized XANES

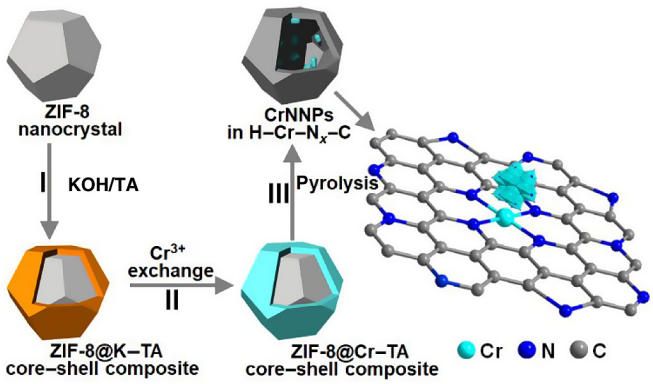

Scheme 1 | *Synthetic scheme for the preparation of CrN@H-Cr-N_x-C.*

DOI: 10.31635/ccschem.020.202000645
CCS Chem. **2021**, *3*, 208–218

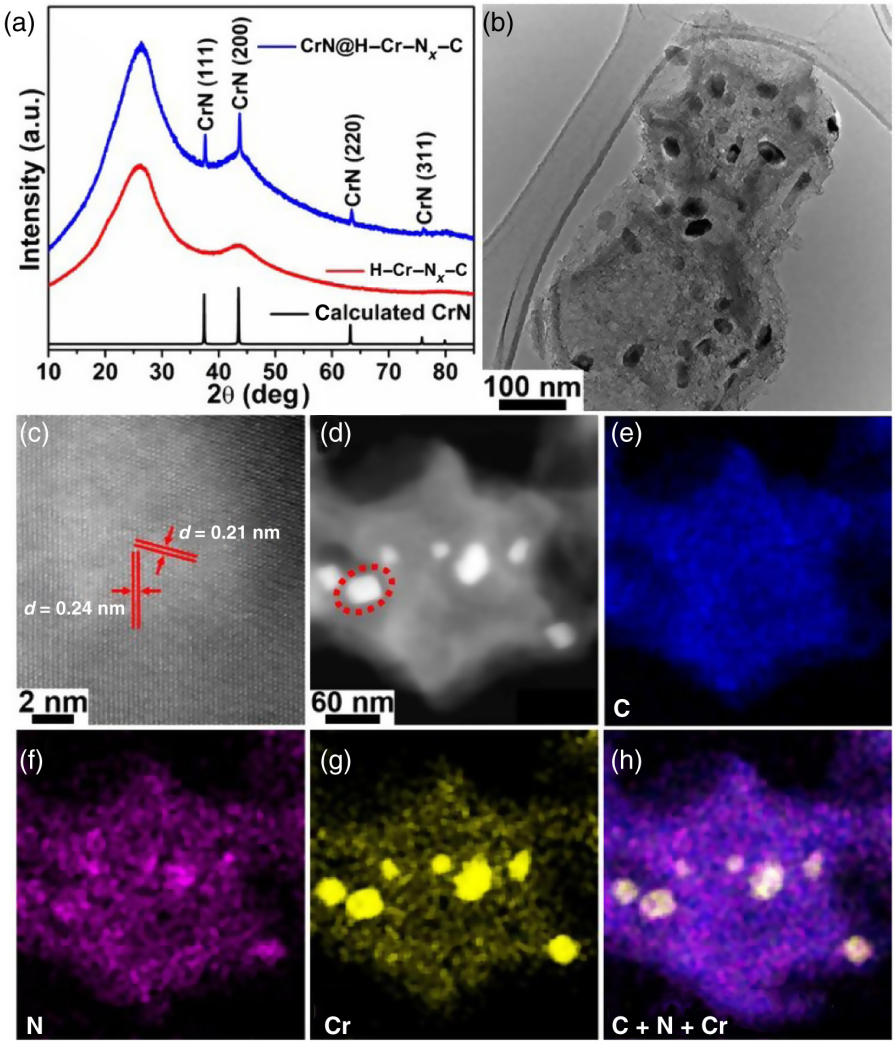

Figure 1 | *(a) PXRD patterns of prepared materials. (b) TEM image of CrN@H–Cr–N$_x$–C. (c) Aberration-corrected HAADF-STEM image of an individual CrN nanoparticle marked with a red-dashed ring in 1 d. (d–h) HAADF-STEM image and EDXS mappings of CrN@H–Cr–N$_x$–C.*

spectra revealed that the Cr *K*-edge absorption edges of CrN@H–Cr–N$_x$–C and H–Cr–N$_x$–C were situated close to that of Cr_2O_3, which corroborated the conclusion obtained from XPS spectra that the chromium sites formed have an oxidation state of approximately 3+ (Figure 3e).[52,53] Moreover, fingerprint peaks at 5991.8 eV were observed in both catalysts, implying that the chromium atoms have been stabilized by strict square-planar configurations with D_{4h} symmetry.[24,45] The EXAFS spectra reveal that the oscillations of CrN@H–Cr–N$_x$–C and H–Cr–N$_x$–C are significantly different compared with Cr foil, Cr_2O_3, and Cr_3C_2 references (Figure 3f). CrN@H–Cr–N$_x$–C and H–Cr–N$_x$–C display a single well-resolved peak at 1.53 Å in *R* space, which implies a Cr–N or Cr–O scattering path.[45,54] The absence of Cr–C and Cr–O second shell scattering paths suggest that no chromium carbide or chromium oxide formed, which is consistent with the presence of Cr–N bonds in these catalysts. Moreover, the EXAFS spectrum of CrN@H–Cr–N$_x$–C shows evidence for Cr–Cr scattering, suggestive of long-range order structure, and the presence of CrN. Therefore, while the XANES spectra point to CrN@H–Cr–N$_x$–C and H–Cr–N$_x$–C being very similar from an electronic structure standpoint, the EXAFS supports the formation of CrNNPs in CrN@H–Cr–N$_x$–C. Fitting the EXAFS data of H–Cr–N$_x$–C to the CrN_4 species was consistent with the isolated chromium centers being coordinated by four nitrogen donors with a Cr–N bond length of 1.94(6) Å (Figure 3h and Supporting Information Table S2). These CrN_4 sites are integrated into porphyrin-like basal planes, as depicted in the computational models (vide infra) (Supporting Information Figure S15a). Based on an arsenal of complementary technologies, we conclude that CrN@H–Cr–N$_x$–C comprises CrNNPs and chromium cations in the 3+ oxidation states coordinated by porphyrin-like four nitrogen atoms without

DOI: 10.31635/ccschem.020.202000645
CCS Chem. **2021**, *3*, 208–218

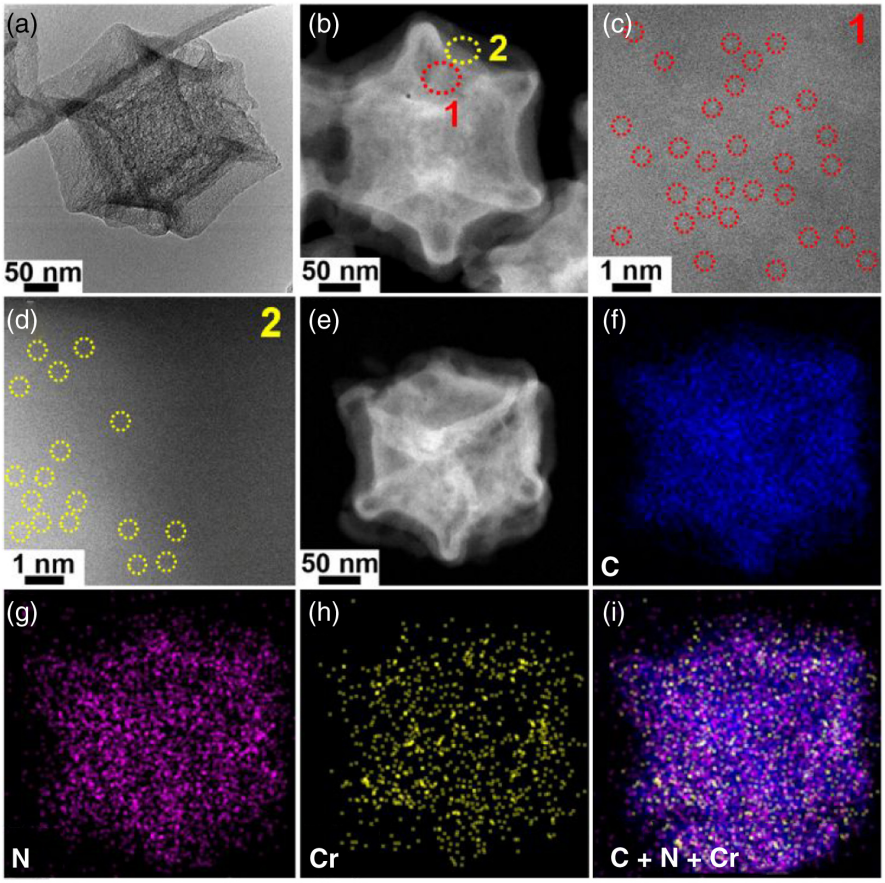

Figure 2 | *(a) TEM image of H-Cr-N_x-C. (b–d) Aberration-corrected HAADF-STEM images of H-Cr-N_x-C. Single Cr atoms are highlighted by red and yellow circles. (e–i) HAADF-STEM image and EDXS mappings of H-Cr-N_x-C.*

axial-bonded oxygen species (Figures 3g and Supporting Information S15d).

CrN@H-Cr-N_x-C is comprised of 7.51 wt % nitrogen, as revealed by elemental analysis (Supporting Information Table S1). H-Cr-N_x-C contains less chromium and more nitrogen (relative proportion) compared with CrN@H-Cr-N_x-C. The Raman spectra of CrN@H-Cr-N_x-C and H-Cr-N_x-C exhibited similar D (1350 cm^{-1}) and G (1590 cm^{-1})-bands, suggesting a similar disorientated degree of graphene (Supporting Information Figure S10). Nitrogen adsorption–desorption isotherms were recorded to probe the accessible porosity of the catalysts at 77 K. The isotherm showed rapid N_2 uptake at a low relative pressure (P/P_0 < 0.1), followed by a more gradual increase at pressures between 0.1 < P/P_0 < 0.95, suggesting that micropores and mesopores are predominant in existence (Figure 3i). Large hysteresis loops were observed at pressures between P/P_0 0.95 and 0.4 during the desorption process, indicating the existence of cavities in these catalysts. The calculated Brunauer–Emmett–Teller (BET) surface areas are 913 and 1054 m^2 g^{-1} for CrN@H-Cr-N_x-C and H-Cr-N_x-C, respectively (Supporting Information Table S1). The pore structures of the catalysts were confirmed by their micropore and mesopore size distributions with void diameters clustered around 1.5 and 2.8 nm, as determined using a DFT model (Supporting Information Figure S8). On this basis, their porosities were expected to offer a higher collision probability of the active sites and reactants without mass transfer limitations, as anticipated for efficient electrocatalysis.

Metal–nitrogen–carbon materials have attracted widespread interest as potential substitutes for PGM catalysts in PEMFC.[7,19,43,48] In this light, CrN@H-Cr-N_x-C and H-Cr-N_x-C were evaluated as electrocatalysts for the PEMFC. First we tested their ORR performance in O_2-saturated 0.1 M $HClO_4$ with RRDE operated at 1600 rpm (Figure 4a). The onset potentials, half-wave potentials, and ultimate current densities calculated from these measurements are shown in Supporting Information Table S3. CrN@H-Cr-N_x-C exhibited a good ORR activity in terms of the onset potential of 0.85 V and a half-wave potential of 0.72 V, which were higher than those of the H-Cr-N_x-C catalyst. The limiting current density of CrN@H-Cr-N_x-C is very close to that of Pt/C (30 wt % of Pt) catalyst. The Tafel slopes of CrN@H-Cr-N_x-C and H-Cr-N_x-C are 57 and 55 mV dec^{-1}, respectively, lower than those of commercial Pt/C (68 mV dec^{-1}), indicating its excellent ORR

DOI: 10.31635/ccschem.020.202000645
CCS Chem. **2021**, *3*, 208–218

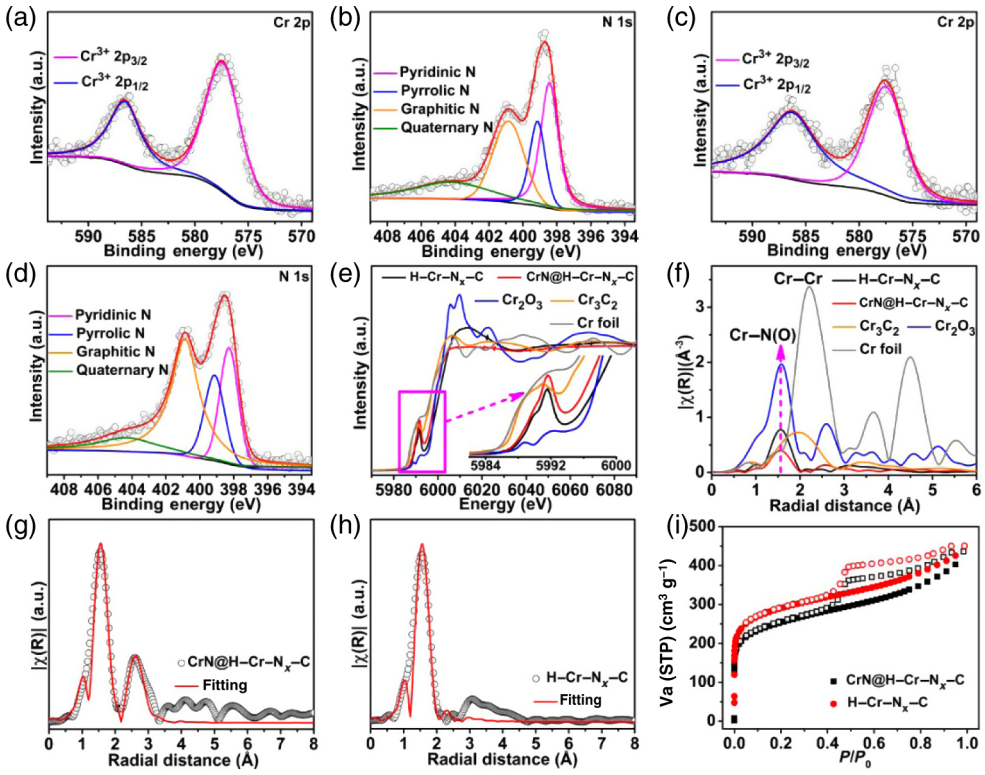

Figure 3 | *(a and b) Cr 2p and N 1s XPS spectra of CrN@H-Cr-N_x-C. (c and d) Cr 2p and N 1s XPS spectra of H-Cr-N_x-C. (e) XANES spectra of CrN@H-Cr-N_x-C and H-Cr-N_x-C together with Cr_3C_2, Cr_2O_3, and Cr foil. (f) Cr* K*-edge Fourier transform (FT) EXAFS spectra of CrN@H-Cr-N_x-C and H-Cr-N_x-C together with Cr_3C_2, Cr_2O_3, and Cr foil. (g and h) Corresponding EXAFS* R *space fitting curves for CrN@H-Cr-Nx-C and H-Cr-Nx-C, respectively. (i) N_2 adsorption and desorption isotherms of catalysts.*

kinetic qualities (Supporting Information Figure S13). Meanwhile, Tafel slopes of both catalysts suggest the same reaction pathway toward the ORR. CrN@H-Cr-N_x-C and H-Cr-N_x-C further showed a low peroxide yield of around 5–20%, and the electron-transfer numbers were found to be 3.9 (Figure 4b). These results suggest the high-efficiency four-electron complete reduction of oxygen to water is preferable[47,55]

RRDE tests preliminarily revealed that the obtained catalysts showed good oxygen reduction activity in acidic solutions. However, the high ORR activity measured from the half-cell does not necessarily imply a high PEMFC performance due to the significantly different working conditions. We further carried out PEMFC performance tests on CrN@H-Cr-N_x-C and H-Cr-N_x-C catalysts. These materials were utilized as cathode materials for fabricating MEAs studied in PEMFCs. The polarization curves were measured by a fuel cell test station (5 cm^2 membrane electrode) at 80 °C and back pressures of 29.4 psi. Commercial Pt/C (30 wt % of Pt on Vulcan XC72 carbo) was used with a loading of 0.2 $mg_{Pt}·cm^{-2}$ as the anode for the H_2 oxidation reaction. Under a catalyst loading of 2 mg cm^{-2}, The OCV measured were 0.85 and 0.75 V for CrN@H-Cr-N_x-C and H-Cr-N_x-C, respectively, in good agreement with RRDE tests in 0.1M $HClO_4$ solutions (Figure 4c). CrN@H-Cr-N_x-C exhibited a current density of 0.888 A·cm^{-2} and a peak power density of 0.382 W·cm^{-2} at 0.43 V, which is higher than those of the MEA made with H-Cr-N_x-C (0.335 A·cm^{-2} and 0.144 W·cm^{-2}). The maximum power density of the cell constructed with CrN@H-Cr-N_x-C was 0.533 W·cm^{-2} at 0.38 V, far superior to the values of 0.28 W·cm^{-2} at 0.32 V for H-Cr-N_x-C. These excellent performances of CrN@H-Cr-N_x-C are comparable with those of other reported M-N_x-C catalysts (Supporting Information Tables S5 and S6). Durability is another important criterion for assessing electrocatalyst performance. M-N_x-C catalysts as cathodes generally exhibited poor stability, with degradability of about 40–80% during the first 100 h of testing in PEMFC.[42-44] However, the CrN@H-Cr-N_x-C exhibited good stability with a current retention rate of 77% over 110 h of operation (Figure 4d).

The above electrochemical measurements indicated that CrN@H-Cr-N_x-C exhibited much superior performance to H-Cr-N_x-C, suggesting that the presence of CrNNPs dramatically boosted the activity of the neighboring CrN_x active sites. Subsequently, DFT calculations were further performed to gain an in-depth

DOI: 10.31635/ccschem.020.202000645
CCS Chem. **2021**, *3*, 208–218

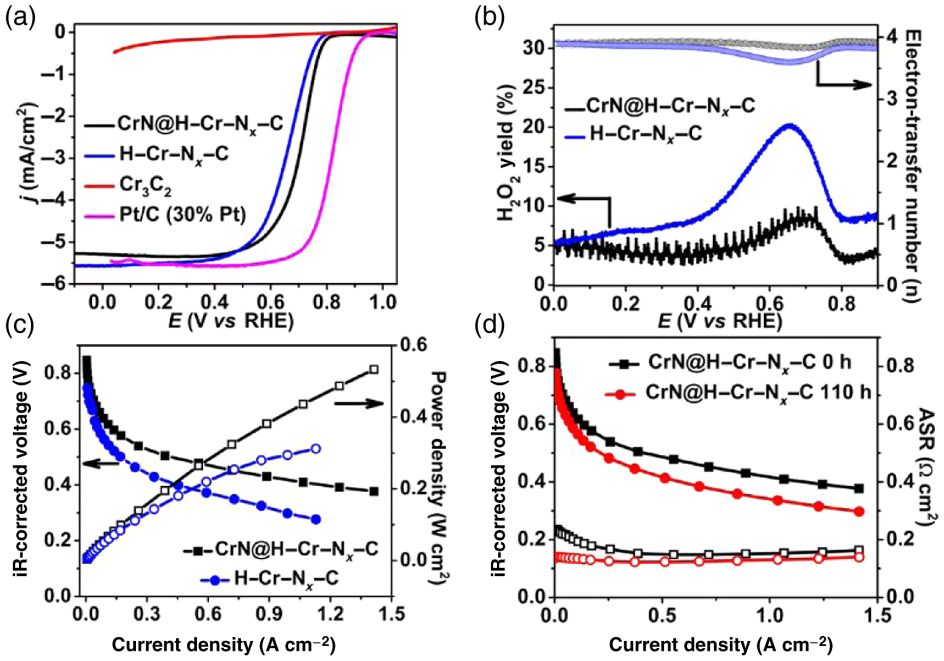

Figure 4 | *(a) Linear sweep voltammetry curves of catalysts. (b) H_2O_2 yield and electron-transfer numbers of catalysts in 0.1 M $HClO_4$ by RRDE tests. (c) I–V polarization and power density curves for H_2–O_2 PEMFC with CrN@H–Cr–N_x–C and H–Cr–N_x–C, respectively, as cathode catalysts at 80 °C. (d) Fuel cell durability tests with CrN@H–Cr–N_x–C as cathode over 110 h operation.*

understanding of the high electrocatalytic performance of CrN@H–Cr–N_x–C. It is well known that an active catalyst can appropriately bind O_2 to initiate the ORR and bind H_2O weakly to complete ORR. Based on the above PXRD, XPS, microscopy, and XAFS results, we considered both the CrN_4 and CrNNPs moieties in CrN@H–Cr–N_x–C as possible active sites for ORR performance. Therefore, structural models of CrN_4 and CrNNPs were calculated for the evaluation (Supporting Information Figures S15–S19, Table S4). We established that both catalysts could complete the reduction of O_2 to H_2O in a four-electron process. By this approach, an O_2 molecule is first adsorbed on a Cr site, then hydrogenated to OOH*, further dissociated into O* and OH*, and finally transformed into H_2O.[56–58] The free-energy diagrams of ORR on these structures are shown in Figure 5a. The ORR on all the structures is spontaneous except for CrN(111) due to its strong adsorption to the intermediates. The adsorption of Cr(100) to the intermediates is relatively weak compared with CrN(111) but is still stronger than H–Cr–N_x–C. The ORR overpotentials of H–Cr–N_x–C, CrN (100), CrN(111), and CrN@H–Cr–N_x–C were calculated to be 0.95, 1.09, 2.88, and 0.19 V, respectively. Compared with H–Cr–N_x–C and CrN configurations, CrN@H–Cr–N_x

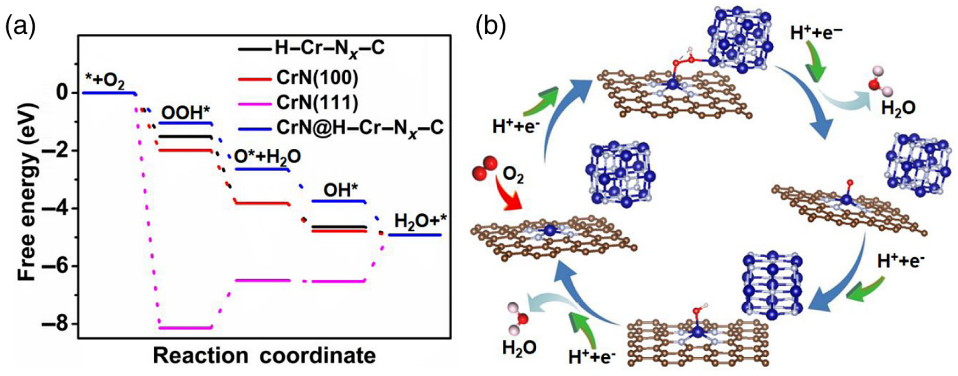

Figure 5 | *(a) The free-energy diagrams of ORR through four-electron pathway in four structures considered in this study. (b) The schematic ORR reaction circle of CrN@H–Cr–N_x–C.*

DOI: 10.31635/ccschem.020.202000645
CCS Chem. **2021**, *3*, 208–218

–C has much lower overpotential, indicating that the presence of CrNNPs can significantly improve the affinity of O_2 and promotes the desorption of OH* on the CrN_4 active sites, thus boosting the ORR activity of the CrN_4 configuration (Figure 5b). The Bader charge and density of states (DOS) are further analyzed in Supporting Information Figures S16 and S17, respectively. The presence of CrN to the H–Cr–N_x–C decreases the positive charge from +1.32 to 1.26 e of CrN_4 catalytic active center in H–Cr–N_x–C, which plays an important role in promoting the desorption of OH*. The high electronic local DOS of the atomically dispersed Cr anchored on hollow N-doped carbon shell in the CrN@H–Cr–N_x–C is close to the Fermi level, which promotes the electronic transfer from metal to absorbates during the reactions and consequently leads to a better catalytic reactivity. This calculation prediction is consistent with the experimental results and helps to explain the excellent experimental ORR performance of CrN@H–Cr–N_x–C in PEMFC.

The above results demonstrate that the CrN@H–Cr–N_x–C is an excellent catalyst for ORR in acidic PEMFC. The excellent electrocatalytic activity of this catalyst can be attributed to: (1) The hollow morphology, electrical conductivity, and porosity of the chromium–nitrogen-doped carbon shell, which have excellent permeability and facilitate the access of O_2 molecules to the catalytic active sites. (2) The atomically dispersed porphyrin-like CrN_x sites are anchored on the walls of hierarchical N-doped porous carbon capsules, which allow for the high exposure and accessibility of active sites. (3) The anchored CrN_x moieties exhibit an inert catalytic activity to the Fenton reaction, thereby leading to good durability. (4) Firm attachment of the embedded CrNNPs to the H–Cr–N_x–C capsules, which provides a large area of exposed contacts between CrNNPs and neighboring CrN_x sites to reduce the O_2 adsorption barrier and improve the OH* desorption capacity during electrocatalytic ORR. This suggests that the activity of CrN_x sites promoted by neighboring CrN nanoparticles.

Conclusion

The CrN@H–Cr–N_x–C has been successfully synthesized. Benefiting from the synergies between CrNNPs and atomically dispersed CrN_x sites, CrN@H–Cr–N_x–C showed very respectable activity for ORR in an acidic electrolyte. Subsequently, the CrN@H–Cr–N_x–C catalyst as a cathode demonstrated excellent initial activity and long-term durability in a PEMFC. DFT calculations further confirmed that the presence of CrN nanoparticles dramatically promoted the active activity of neighboring CrN_x sites for ORR in PEMFC. This suggests that a promising future awaits this class of materials as ORR electrocatalysts in PEMFC. The strategy reported here for the synthesis of these catalysts is straightforward and uses earth-abundant precursors. This study paves a new way for the design of robust catalysts for electrolytic applications.

Supporting Information

Supporting Information is available and includes chemicals, instrumentation, experimental procedures, PXRD, SEM, TEM, EDXS, pore size analysis, FT-IR, Raman, XPS, XAFS, ORR related curves and calculations, and DFT calculations.

Conflict of Interest

The authors declare no conflict of interest.

Acknowledgments

The authors gratefully acknowledge the support from the Robert A. Welch Foundation (B-0027) (S.M.). Support from North China Electric Power University (no. XM2009903) and the National Science Foundation of China (grant no. 22006036) are also acknowledged (H.Y. and X.W.). R.W.M. and J.T.W. acknowledge support from the U.S. National Science Foundation (no. DMR-1708617). Materials Research Collaborative Access Team (MRCAT) operations are supported by the Department of Energy (DOE) and the MRCAT member institutions. This research used resources of the Advanced Photon Source, a U.S. DOE Office of Science User Facility operated for the DOE Office of Science by Argonne National Laboratory under Contract no. DE-AC02-06CH11357.

References

1. Debe, M. K. Electrocatalyst Approaches and Challenges for Automotive Fuel Cells. *Nature* **2012**, *486*, 43–51.
2. Morozan, A.; Jousselme, B.; Palacin, S. Low-Platinum and Platinum-Free Catalysts for the Oxygen Reduction Reaction at Fuel Cell Cathodes. *Energy Environ. Sci.* **2011**, *4*, 1238–1254.
3. Zhang, S.; Yuan, X.-Z.; Hin, J. N. C.; Wang, H.; Friedrich, K. A.; Schulze, M. A Review of Platinum-Based Catalyst Layer Degradation in Proton Exchange Membrane Fuel Cells. *J. Power Sources* **2009**, *194*, 588–600.
4. Chung, D. Y.; Yoo, J. M.; Sung, Y. E. Highly Durable and Active Pt-Based Nanoscale Design for Fuel-Cell Oxygen-Reduction Electrocatalysts. *Adv. Mater.* **2018**, *30*, 1704123.
5. Wang, Y.-J.; Long, W.; Wang, L.; Yuan, R.; Ignaszak, A.; Fang, B.; Wilkinson, D. P. Unlocking the Door to Highly Active ORR Catalysts for PEMFC Applications: Polyhedron-Engineered Pt-Based Nanocrystals. *Energy Environ. Sci.* **2018**, *11*, 258–275.
6. Shao, M.; Chang, Q.; Dodelet, J. P.; Chenitz, R. Recent Advances in Electrocatalysts for Oxygen Reduction Reaction. *Chem. Rev.* **2016**, *116*, 3594–3657.

7. Zhang, L.; Wilkinson, D. P.; Liu, Y.; Zhang, J. Progress in Nanostructured (Fe or Co)/N/C Non-Noble Metal Electrocatalysts for Fuel Cell Oxygen Reduction Reaction. *Electrochim. Acta* **2018**, *262*, 326–336.
8. Sahraie, N. R.; Kramm, U. I.; Steinberg, J.; Zhang, Y.; Thomas, A.; Reier, T.; Paraknowitsch, J. P.; Strasser, P. Quantifying the Density and Utilization of Active Sites in Non-Precious Metal Oxygen Electroreduction Catalysts. *Nat. Commun.* **2015**, *6*, 8618.
9. Liu, Q.; Liu, X.; Zheng, L.; Shui, J. The Solid-Phase Synthesis of an Fe-N-C Electrocatalyst for High-Power Proton-Exchange Membrane Fuel Cells. *Angew. Chem. Int. Ed.* **2018**, *57*, 1204–1208.
10. Chung, H. T.; Cullen, D. A.; Higgins, D.; Sneed, B. T.; Holby, E. F.; More, K. L.; Zelenay, P. Direct Atomic-Level Insight into the Active Sites of a High-Performance PGM-Free ORR Catalyst. *Science* **2017**, *357*, 479–484.
11. Meng, F. L.; Wang, Z. L.; Zhong, H. X.; Wang, J.; Yan, J. M.; Zhang, X. B. Reactive Multifunctional Template-Induced Preparation of Fe-N-Doped Mesoporous Carbon Microspheres towards Highly Efficient Electrocatalysts for Oxygen Reduction. *Adv. Mater.* **2016**, *28*, 7948–7955.
12. Zhao, D.; Shui, J. L.; Grabstanowicz, L. R.; Chen, C.; Commet, S. M.; Xu, T.; Lu, J.; Liu, D. J. Highly Efficient Non-Precious Metal Electrocatalysts Prepared from One-Pot Synthesized Zeolitic Imidazolate Frameworks. *Adv. Mater.* **2014**, *26*, 1093–1097.
13. Wang, X. X.; Cullen, D. A.; Pan, Y.-T.; Hwang, S.; Wang, M.; Feng, Z.; Wang, J.; Engelhard, M. H.; Zhang, H.; He, Y.; Shao, Y.; Su, D.; More, K. L.; Spendelow, J. S.; Wu, G. Nitrogen-Coordinated Single Cobalt Atom Catalysts for Oxygen Reduction in Proton Exchange Membrane Fuel Cells. *Adv. Mater.* **2018**, *30*, 1706758.
14. Ma, S.; Goenaga, G. A.; Call, A. V.; Liu, D. J. Cobalt Imidazolate Framework as Precursor for Oxygen Reduction Reaction Electrocatalysts. *Chem. Eur. J.* **2011**, *17*, 2063–2067.
15. Shui, J.; Chen, C.; Grabstanowicz, L.; Zhao, D.; Liu, D. J. Highly Efficient Nonprecious Metal Catalyst Prepared with Metal-Organic Framework in a Continuous Carbon Nanofibrous Network. *Proc. Natl. Acad. Sci. U. S. A.* **2015**, *112*, 10629–10634.
16. Zhao, R.; Liang, Z.; Gao, S.; Yang, C.; Zhu, B.; Zhao, J.; Qu, C.; Zou, R.; Xu, Q. Puffing Up Energetic Metal-Organic Frameworks to Large Carbon Networks with Hierarchical Porosity and Atomically Dispersed Metal Sites. *Angew. Chem. Int. Ed.* **2019**, *58*, 1975–1979.
17. Jiao, L.; Wan, G.; Zhang, R.; Zhou, H.; Yu, S. H.; Jiang, H. L. From Metal-Organic Frameworks to Single-Atom Fe Implanted N-Doped Porous Carbons: Efficient Oxygen Reduction in Both Alkaline and Acidic Media. *Angew. Chem. Int. Ed.* **2018**, *57*, 8525–8529.
18. Li, J.; Chen, M.; Cullen, D. A.; Hwang, S.; Wang, M.; Li, B.; Liu, K.; Karakalos, S.; Lucero, M.; Zhang, H.; Lei, C.; Xu, H.; Sterbinsky, G. E.; Feng, Z.; Su, D.; More, K. L.; Wang, G.; Wang, Z.; Wu, G. Atomically Dispersed Manganese Catalysts for Oxygen Reduction in Proton-Exchange Membrane Fuel Cells. *Nat. Catal.* **2018**, *1*, 935–945.
19. Masa, J.; Xia, W.; Muhler, M.; Schuhmann, W. On the Role of Metals in Nitrogen-Doped Carbon Electrocatalysts for Oxygen Reduction. *Angew. Chem. Int. Ed.* **2015**, *54*, 10102–10120.
20. Liang, H. W.; Wei, W.; Wu, Z. S.; Feng, X.; Mullen, K. Mesoporous Metal-Nitrogen-Doped Carbon Electrocatalysts for Highly Efficient Oxygen Reduction Reaction. *J. Am. Chem. Soc.* **2013**, *135*, 16002–16005.
21. Zitolo, A.; Ranjbar-Sahraie, N.; Mineva, T.; Li, J.; Jia, Q.; Stamatin, S.; Harrington, G. F.; Lyth, S. M.; Krtil, P.; Mukerjee, S.; Fonda, E.; Jaouen, F. Identification of Catalytic Sites in Cobalt-Nitrogen-Carbon Materials for the Oxygen Reduction Reaction. *Nat. Commun.* **2017**, *8*, 957.
22. Tian, J.; Morozan, A.; Sougrati, M. T.; Lefevre, M.; Chenitz, R.; Dodelet, J. P.; Jones, D.; Jaouen, F. Optimized Synthesis of Fe/N/C Cathode Catalysts for PEM Fuel Cells: A Matter of Iron-Ligand Coordination Strength. *Angew. Chem. Int. Ed.* **2013**, *52*, 6867–6870.
23. Fu, X.; Li, N.; Ren, B.; Jiang, G.; Liu, Y.; Hassan, F. M.; Su, D.; Zhu, J.; Yang, L.; Bai, Z.; Cano, Z. P.; Yu, A.; Chen, Z. Tailoring FeN_4 Sites with Edge Enrichment for Boosted Oxygen Reduction Performance in Proton Exchange Membrane Fuel Cell. *Adv. Eng. Mater.* **2019**, *9*, 1803737.
24. Yang, H.; Chen, X.; Chen, W. T.; Wang, Q.; Cuello, N. C.; Nafady, A.; Al-Enizi, A. M.; Waterhouse, G. I. N.; Goenaga, G. A.; Zawodzinski, T. A.; Kruger, P. E.; Clements, J. E.; Zhang, J.; Tian, H.; Telfer, S. G.; Ma, S. Tunable Synthesis of Hollow Metal-Nitrogen-Carbon Capsules for Efficient Oxygen Reduction Catalysis in Proton Exchange Membrane Fuel Cells. *ACS Nano* **2019**, *13*, 8087–8098.
25. Zhao, L.; Zhang, Y.; Huang, L. B.; Liu, X. Z.; Zhang, Q. H.; He, C.; Wu, Z. Y.; Zhang, L. J.; Wu, J.; Yang, W.; Gu, L.; Hu, J. S.; Wan, L. J. Cascade Anchoring Strategy for General Mass Production of High-Loading Single-Atomic Metal-Nitrogen Catalysts. *Nat. Commun.* **2019**, *10*, 1278.
26. Chen, Y.; Ji, S.; Wang, Y.; Dong, J.; Chen, W.; Li, Z.; Shen, R.; Zheng, L.; Zhuang, Z.; Wang, D.; Li, Y. Isolated Single Iron Atoms Anchored on N-Doped Porous Carbon as an Efficient Electrocatalyst for the Oxygen Reduction Reaction. *Angew. Chem. Int. Ed.* **2017**, *56*, 6937–6941.
27. Wang, J.; Huang, Z.; Liu, W.; Chang, C.; Tang, H.; Li, Z.; Chen, W.; Jia, C.; Yao, T.; Wei, S.; Wu, Y.; Li, Y. Design of N-Coordinated Dual-Metal Sites: A Stable and Active Pt-Free Catalyst for Acidic Oxygen Reduction Reaction. *J. Am. Chem. Soc.* **2017**, *139*, 17281–17284.
28. Zhu, C.; Shi, Q.; Xu, B. Z.; Fu, S.; Wan, G.; Yang, C.; Yao, S.; Song, J.; Zhou, H.; Du, D.; Beckman, S. P.; Su, D.; Lin, Y. Hierarchically Porous M-N-C (M = Co and Fe) Single-Atom Electrocatalysts with Robust MNx Active Moieties Enable Enhanced ORR Performance. *Adv. Eng. Mater.* **2018**, *8*, 1801956.
29. Chen, Y.; Li, Z.; Zhu, Y.; Sun, D.; Liu, X.; Xu, L.; Tang, Y. Atomic Fe Dispersed on N-Doped Carbon Hollow Nanospheres for High-Efficiency Electrocatalytic Oxygen Reduction. *Adv. Mater.* **2019**, *31*, 1806312.
30. Workman, M. J.; Serov, A.; Tsui, L.-k.; Atanassov, P.; Artyushkova, K. Fe–N–C Catalyst Graphitic Layer Structure

and Fuel Cell Performance. *ACS Energy Lett.* **2017**, *2*, 1489–1493.
31. Sa, Y. J.; Seo, D. J.; Woo, J.; Lim, J. T.; Cheon, J. Y.; Yang, S. Y.; Lee, J. M.; Kang, D.; Shin, T. J.; Shin, H. S.; Jeong, H. Y.; Kim, C. S.; Kim, M. G.; Kim, T. Y.; Joo, S. H. A General Approach to Preferential Formation of Active Fe-Nx Sites in Fe-N/C Electrocatalysts for Efficient Oxygen Reduction Reaction. *J. Am. Chem. Soc.* **2016**, *138*, 15046–15056.
32. Zhang, H.; Hwang, S.; Wang, M.; Feng, Z.; Karakalos, S.; Luo, L.; Qiao, Z.; Xie, X.; Wang, C.; Su, D.; Shao, Y.; Wu, G. Single Atomic Iron Catalysts for Oxygen Reduction in Acidic Media: Particle Size Control and Thermal Activation. *J. Am. Chem. Soc.* **2017**, *139*, 14143–14149.
33. Lin, Q.; Bu, X.; Kong, A.; Mao, C.; Bu, F.; Feng, P. Heterometal-Embedded Organic Conjugate Frameworks from Alternating Monomeric Iron and Cobalt Metalloporphyrins and Their Application in Design of Porous Carbon Catalysts. *Adv. Mater.* **2015**, *27*, 3431–3436.
34. Ao, X.; Zhang, W.; Li, Z.; Lv, L.; Ruan, Y.; Wu, H.-H.; Chiang, W.-H.; Wang, C.; Liu, M.; Zeng, X. C. Unraveling the High-Activity Nature of Fe–N–C Electrocatalysts for the Oxygen Reduction Reaction: The Extraordinary Synergy Between Fe–N_4 and Fe_4N. *J. Mater. Chem. A* **2019**, *7*, 11792–11801.
35. Jiang, W. J.; Gu, L.; Li, L.; Zhang, Y.; Zhang, X.; Zhang, L. J.; Wang, J. Q.; Hu, J. S.; Wei, Z.; Wan, L. J. Understanding the High Activity of Fe-N-C Electrocatalysts in Oxygen Reduction: Fe/Fe_3C Nanoparticles Boost the Activity of Fe-N(x). *J. Am. Chem. Soc.* **2016**, *138*, 3570–3578.
36. Chong, L.; Wen, J.; Kubal, J.; Sen, F. G.; Zou, J.; Greeley, J.; Chan, M.; Barkholtz, H.; Ding, W.; Liu, D. J. Ultralow-Loading Platinum-Cobalt Fuel Cell Catalysts Derived from Imidazolate Frameworks. *Science* **2018**, *362*, 1276–1281.
37. Chen, M. X.; Zhu, M.; Zuo, M.; Chu, S. Q.; Zhang, J.; Wu, Y.; Liang, H. W.; Feng, X. Identification of Catalytic Sites for Oxygen Reduction in Metal/Nitrogen-Doped Carbons with Encapsulated Metal Nanoparticles. *Angew. Chem. Int. Ed.* **2020**, *59*, 1627–1633.
38. Wang, H.; Yin, F. X.; Liu, N.; Kou, R. H.; He, X. B.; Sun, C. J.; Chen, B. H.; Liu, D. J.; Yin, H. Q. Engineering Fe–Fe_3C@Fe–N–C Active Sites and Hybrid Structures from Dual Metal–Organic Frameworks for Oxygen Reduction Reaction in H_2–O_2 Fuel Cell and Li–O_2 Battery. *Adv. Funct. Mater.* **2019**, *29*, 1901531.
39. Tylus, U.; Jia, Q.; Strickland, K.; Ramaswamy, N.; Serov, A.; Atanassov, P.; Mukerjee, S. Elucidating Oxygen Reduction Active Sites in Pyrolyzed Metal-Nitrogen Coordinated Non-Precious-Metal Electrocatalyst Systems. *J. Phys. Chem. C* **2014**, *118*, 8999–9008.
40. Li, Z.; Zhuang, Z.; Lv, F.; Zhu, H.; Zhou, L.; Luo, M.; Zhu, J.; Lang, Z.; Feng, S.; Chen, W.; Mai, L.; Guo, S. The Marriage of the FeN_4 Moiety and MXene Boosts Oxygen Reduction Catalysis: Fe 3d Electron Delocalization Matters. *Adv. Mater.* **2018**, *30*, 1803220.
41. Li, B.; Zhang, L.; Chen, L.; Cai, X.; Lai, L.; Wang, Z.; Shen, Z.; Lin, J. Graphene-Supported Non-Precious Metal Electrocatalysts for Oxygen Reduction Reactions: The Active Center and Catalytic Mechanism. *J. Mater. Chem. A* **2016**, *4*, 7148–7154.
42. Proietti, E.; Jaouen, F.; Lefevre, M.; Larouche, N.; Tian, J.; Herranz, J.; Dodelet, J. P. Iron-Based Cathode Catalyst with Enhanced Power Density in Polymer Electrolyte Membrane Fuel Cells. *Nat. Commun.* **2011**, *2*, 416.
43. Shao, Y.; Dodelet, J. P.; Wu, G.; Zelenay, P. PGM-Free Cathode Catalysts for PEM Fuel Cells: A Mini-Review on Stability Challenges. *Adv. Mater.* **2019**, *31*, 1807615.
44. Martinez, U.; Komini Babu, S.; Holby, E. F.; Zelenay, P. Durability Challenges and Perspective in the Development of PGM-Free Electrocatalysts for the Oxygen Reduction Reaction. *Curr. Opin. Electrochem.* **2018**, *9*, 224–232.
45. Luo, E.; Zhang, H.; Wang, X.; Gao, L.; Gong, L.; Zhao, T.; Jin, Z.; Ge, J.; Jiang, Z.; Liu, C.; Xing, W. Single-Atom Cr-N4 Sites Designed for Durable Oxygen Reduction Catalysis in Acid Media. *Angew. Chem. Int. Ed.* **2019**, *58*, 12469–12475.
46. Choi, C. H.; Lim, H.-K.; Chung, M. W.; Chon, G.; Ranjbar Sahraie, N.; Altin, A.; Sougrati, M.-T.; Stievano, L.; Oh, H. S.; Park, E. S.; Luo, F.; Strasser, P.; Dražić, G.; Mayrhofer, K. J. J.; Kim, H.; Jaouen, F. The Achilles' Heel of Iron-Based Catalysts During Oxygen Reduction in an Acidic Medium. *Energy Environ. Sci.* **2018**, *11*, 3176–3182.
47. Cantillo, N. M.; Goenaga, G. A.; Gao, W.; Williams, K.; Neal, C. A.; Ma, S.; More, K. L.; Zawodzinski, T. A. Investigation of a Microporous Iron(III) Porphyrin Framework Derived Cathode Catalyst in PEM Fuel Cells. *J. Mater. Chem. A* **2016**, *4*, 15621–15630.
48. Martinez, U.; Komini Babu, S.; Holby, E. F.; Chung, H. T.; Yin, X.; Zelenay, P. Progress in the Development of Fe-Based PGM-Free Electrocatalysts for the Oxygen Reduction Reaction. *Adv. Mater.* **2019**, *31*, 1806545.
49. Yang, H.; Bradley, S. J.; Chan, A.; Waterhouse, G. I.; Nann, T.; Kruger, P. E.; Telfer, S. G. Catalytically Active Bimetallic Nanoparticles Supported on Porous Carbon Capsules Derived from Metal-Organic Framework Composites. *J. Am. Chem. Soc.* **2016**, *138*, 11872–11881.
50. Idrees, M.; Abbas, S. M.; Ata Ur, R.; Ahmad, N.; Mushtaq, M. W.; Naqvi, R. A.; Nam, K.-W.; Muhammad, B.; Iqbal, Z. Mechanistic Insights into High Lithium Storage Performance of Mesoporous Chromium Nitride Anchored on Nitrogen-Doped Carbon Nanotubes. *Chem. Eng. J.* **2017**, *327*, 361–370.
51. Abbas, S. M.; Ahmad, N.; Ur-Rahman, A.; Rana, U. A.; Khan, S. U.-D.; Hussain, S.; Nam, K.-W. High Rate Capability and Long Cycle Stability of Cr_2O_3 Anode with CNTs for Lithium Ion Batteries. *Electrochim. Acta* **2016**, *212*, 260–269.
52. Pedersen, K. S.; Perlepe, P.; Aubrey, M. L.; Woodruff, D. N.; Reyes-Lillo, S. E.; Reinholdt, A.; Voigt, L.; Li, Z.; Borup, K.; Rouzieres, M.; Samohvalov, D.; Wilhelm, F.; Rogalev, A.; Neaton, J. B.; Long, J. R.; Clerac, R. Formation of the Layered Conductive Magnet $CrCl_2$(pyrazine)$_2$ through Redox-Active Coordination Chemistry. *Nat. Chem.* **2018**, *10*, 1056–1061.
53. Pantelouris, A.; Modrow, H.; Pantelouris, M.; Hormes, J.; Reinen, D. The Influence of Coordination Geometry and Valency on the K-Edge Absorption Near Edge Spectra of Selected Chromium Compounds. *Chem. Phys.* **2004**, *300*, 13–22.

DOI: 10.31635/ccschem.020.202000645
CCS Chem. **2021**, *3*, 208–218

54. Panda, P.; Ramaseshan, R.; Sahoo, M.; Krishna, N. G.; Yadav, A. K.; Jha, S. N.; Bhattacharyya, D. Local Crystal Structure in the Vicinity of Cr in Doped AlN Thin Films Studied by X-ray Absorption Spectroscopy. *Phys. Chem. Chem. Phys.* **2018**, *20*, 13084–13091.
55. Gokhale, R.; Chen, Y.; Serov, A.; Artyushkova, K.; Atanassov, P. Novel Dual Templating Approach for Preparation of Highly Active Fe-N-C Electrocatalyst for Oxygen Reduction. *Electrochim. Acta* **2017**, *224*, 49–55.
56. Liu, K.; Kattel, S.; Mao, V.; Wang, G. Electrochemical and Computational Study of Oxygen Reduction Reaction on Nonprecious Transition Metal/Nitrogen Doped Carbon Nanofibers in Acid Medium. *J. Phys. Chem. C* **2016**, *120*, 1586–1596.
57. Norskov, J. K.; Rossmeisl, J.; Logadottir, A.; Lindqvist, L.; Kitchin, J. R.; Bligaard, T.; Jonsson, H. Origin of the Overpotential for Oxygen Reduction at a Fuel-Cell Cathode. *J. Phys. Chem. B* **2004**, *108*, 17886–17892.
58. Li, M.; Zhang, L.; Xu, Q.; Niu, J.; Xia, Z. N-Doped Graphene as Catalysts for Oxygen Reduction and Oxygen Evolution Reactions: Theoretical Considerations. *J. Catal.* **2014**, *314*, 66–72.

DOI: 10.31635/ccschem.020.202000645
CCS Chem. **2021**, *3*, 208–218